

## Supplementary Information:

### **Electrospun TiO<sub>2</sub>/carbon composite nanofibers as effective (photo)electrodes for removal and transformation of recalcitrant water contaminants**

Ashley Hesterberg Butzlaff,<sup>a</sup> Madeline Jensen,<sup>a</sup> Chenxu Yan,<sup>b</sup> Sattar Al Saedi,<sup>c</sup> Charles Werth,<sup>b</sup> David Cwiertny,<sup>\*a</sup> and Syed Mubeen<sup>\*c</sup>

<sup>a</sup> Department of Civil and Environmental Engineering, University of Iowa, Iowa City, Iowa 52242, United States

<sup>b</sup> Department of Civil, Architectural, and Environmental Engineering, The University of Texas at Austin, 301 E. Dean Keeton St, Stop C1786, Austin, Texas 78712-1173

<sup>c</sup> Department of Chemical and Biochemical Engineering, University of Iowa, Iowa City, Iowa 52242, United States

\* Corresponding authors E-mail: [david-cwiertny@uiowa.edu](mailto:david-cwiertny@uiowa.edu); [syed-mubeen@uiowa.edu](mailto:syed-mubeen@uiowa.edu)

In preparation for submission to *Environmental Science: Advances*

13 figures, 6 tables

## SUPPLEMENTAL MATERIALS AND METHODS

### Reagents

All reagents were used as received. The electrospinning precursor solutions were synthesized with polyacrylonitrile (PAN; MW 150,000, Aldrich), phthalic acid (PTA; Aldrich), titanium (IV) oxide (Aeroxide P25, Evonik), and N,N-dimethylformamide (DMF; 99.85%, BDH Chemicals). Aeroxide P25 is a crystalline nanopowder mixture (approximately 75 wt. % anatase, 25 wt. % rutile) synthesized by vaporizing titanium tetrachloride, mixing with air and hydrogen, and reacting at high temperature in a burner.<sup>1</sup> Potentiostatic electrochemical impedance spectroscopy (PEIS) and transformation experiments were carried out in 0.5 M potassium buffer (anhydrous potassium phosphate monobasic,  $\text{KH}_2\text{PO}_4$ ; and dibasic,  $\text{K}_2\text{HPO}_4$ ; Research Products International) prepared from deionized water and pH-adjusted to neutral pH with phosphoric acid (85 wt% aqueous solution; Aldrich) if needed. For transformation experiments, carbamazepine (CBZ; Aldrich) was added to 0.5 M phosphate buffer, neutral pH.

### Electrode synthesis

Solution preparation and electrospinning. Electrospun CNF electrodes were derived from a sol gel containing PAN (8 wt. % relative to total solution mass) as the polymer precursor and DMF as the suspending solvent. Based on our previous work, PTA was included to produce mechanically stable and durable CNFs with increased flexibility and introduced porosity.<sup>2</sup> Precursor solution composition (**Figure S1**) was determined by the following:

$$m_{PTA}(g) = \frac{wt\%_{PTA} * [m_{P25}(g) + m_{PAN}(g) + V_{DMF}(mL) * \rho_{DMF}(\frac{g}{mL})]}{(100 - wt\%_{PTA})} \quad (1)$$

$$wt\%_{P25} = \frac{m_{P25}(g)}{(m_{P25}(g) + m_{PAN}(g))} \quad (2)$$

First, TiO<sub>2</sub> and PTA were mixed with DMF followed by ultrasonication (Branson 510) for five hours prior to the dissolution of PAN. Second, PAN was added to the suspended TiO<sub>2</sub> and thermomixed for 2 hours at 60 °C and 700 rpm. Precursor solutions were stored in capped vials on an end-over-end rotator after sonication (Branson 510) and/or thermomixing (Eppendorf ThermoMixer C). If not used immediately after preparation, solutions were thermomixed again for 30 minutes at 60 °C and 700 rpm prior to electrospinning to remove any remaining solid PAN. The solution was then transferred to a 12 mL plastic syringe (HSW Norm-Ject), which was connected to 2.0 mm ID polyethylene (PE) tubing via a PE 1/16" female luer lock fitting (NanoNC Co., Ltd). The fitting was secured to a metal nozzle adapter (Nano NC, Korea) while the opposite end of the nozzle adapter was connected to a 1/4" metal dispensing needle (JG23-0.25HPX, Jensen Global). The nozzle was secured in a custom-made stand. The solution was pumped through the tubing, nozzle adapter, and needle at a rate of 0.5 mL/h via a syringe pump (New Era Pump Systems, Inc.). After exiting from the needle, the solution entered an electric field, produced from a positive applied electric potential difference of 15 kV (high voltage AC to DC converter, Acopian). The applied potential between the needle tip and the grounded rotating metal drum collector (SPG Co., Ltd, Korea, 9-5/16" circumference, approximately 600 rpm) causes CNF deposition by forming a whipping jet at the needle tip and evaporating the solvent. Nanofibers were deposited on aluminum foil covering the rotating drum collector. Needle tip was positioned 10 cm

from the rotating metal drum collector. The total time for electrospinning (1.5-7 h) depended on solvent volume, as determined by the sol-gel formula.

Stabilization and carbonization. Oxidative stabilization and carbonization (**Figure S4**) were carried out in a programmable tube furnace (MTI Corporation, OTF-1200X-UL) with a quartz tube (90 mm diameter). Temperature programming was achieved with the built-in high precision digital controller ( $\pm 1$  °C). Although the controller is highly accurate, the heating zone exhibits a temperature distribution across the length of the tube. Samples were centered in the furnace below the thermocouple, where temperature reached its maximum and closest value to the set value. The actual temperature varied from the set temperature by approximately  $\pm 45$  °C. Therefore, the temperature intervals employed here (450, 575, 750 and 1000 °C) ensure distinctly different carbonization temperatures.

### **Nanofiber characterization**

Physical properties. Specific surface area ( $S_{\text{BET}}$ ) was determined from multi-point BET, where relative pressures ( $P/P_0$ ) ranged from  $0.05 \leq P/P_0 \leq 0.33$ . The t-plot ( $V-t$ , where  $V$  is the volume of gas adsorbed and  $t$  is the statistical film thickness) method was applied to the adsorption isotherm to determine micropore volume and surface area.<sup>3-5</sup> The Barrett, Joyner, and Halenda (BJH) method was applied to the desorption isotherm to determine mesopore surface area and volume.<sup>5-7</sup> Total pore volume was estimated at  $P/P_0 \approx 0.95$ .

Crystal structures for  $\text{TiO}_2$  and carbon were identified with XRD and Raman, respectively. Powder XRD employed a Cu radiation source ( $\lambda = 1.54$  Å) operating at 40 kV and 40 mA (Bruker D-5000 q - q diffractometer). Diffraction

response was analyzed from 10 to 60° at a rate of 1°/min ( $2\theta$ ). The strongest diffraction lines for the anatase ( $2\theta = 25.2^\circ$ ) and rutile ( $2\theta = 27.4^\circ$ ) structures were referenced to compare shifts in crystal structure with carbonization temperature. Raman operated with a 514 nm diode light source at 50% power to avoid sample degradation. Raman spectra were collected at 50x magnification with a 1800 l mm<sup>-1</sup> grating, 1420 cm<sup>-1</sup> center wavelength, 30 s exposure time, and 10 accumulations. After baseline correction, the spectra were normalized using the min/max method.

For bulk (macroscale) tensile strength (Young's modulus, kg/mm<sup>2</sup>), a total of six coupons were tested per fiber type (3 lengthwise, 3 widthwise). Samples were cut and tested directionally because the nonwoven nature of the CNF composites suggested direction-dependent (anisotropic) strength. Square tabs of aluminum foil were placed at sample ends to prevent damage to the sample during grip tightening. The use of aluminum foil at the grips followed the method for tensile testing of PAN-based carbon matrix composites.<sup>8</sup>

*Electrochemical properties.* For potentiostatic electrochemical impedance spectroscopy (PEIS) measurements, the electrode sample was attached to a glass slide with insulating tape and inserted into the Teflon microreactor with electrolyte volume of 1.5 mL and an exposed geometric surface area of 0.5 cm<sup>2</sup> (**Figure S6**). A stable open circuit voltage ( $E_{oc}$ ) less than  $\pm 300$  millivolts was established prior to each measurement. **Table S1** provides the experimental parameters used to collect the reported PEIS data.

### **CBZ analytical methods**

The 1100 Series Agilent HPLC-DAD was equipped with an Eclipse XDB-C18 column (4.6 × 50 mm, 1.8 μm particle size). Carbamazepine was analyzed based on a previously determined HPLC method with the following parameters: mobile phase of 55:45 DI water: ACN, flow rate of 1 mL/min, an injection volume of 25 μL, and a 213 nm detection wavelength.<sup>9</sup> Samples were extracted (700 μL/sample) during the 90-minute transformation period for HPLC analysis.

## SUPPLEMENTAL RESULTS AND DISCUSSION

### Electrode properties

Bulk structural properties across carbonization temperatures. **Figure S10** provides the adsorption-desorption N<sub>2</sub> isotherms and the resulting pore distribution for the 0.45 g PAN / 50 wt% TiO<sub>2</sub> composites carbonized at 450 and 1000 °C. The isotherms (**Figure S10a**) revealed Type H4 hysteresis for samples carbonized at 450 °C and Type H3 hysteresis for samples carbonized at 1000 °C [according to the International Union of Pure and Applied Chemistry (IUPAC)<sup>10</sup>]. IUPAC defines type H3 hysteresis by no adsorption limits at high P/P<sub>0</sub> and a forced return of the desorption branch to the adsorption branch, which occurs at approximately P/P<sub>0</sub> ≈ 0.42 for N<sub>2</sub> isotherms at 77 K. Type H4 hysteresis is defined by almost horizontal and parallel branches across a wide P/P<sub>0</sub> range. While both H4 and H3 hysteresis patterns indicate slit-like pore structures, the shift in isotherm character demonstrated that pore structures become less narrow (less microporous) with increasing carbonization temperature.

The distinct isotherm character with temperature is supported by the mesopore distribution as determined by the Barrett, Joyner, and Halenda (BJH) method, which assumes cylindrical pore geometry.<sup>5-7</sup> As shown in **Figures S10b** and **S10c**, composites carbonized at 1000 °C exhibit greater cumulative pore volume and more pore volume at larger pore sizes. This is corroborated by the increase in the surface area observed with increasing carbonization temperature, where the multi-point BET surface area (S<sub>BET</sub>) increased by 1.75-fold and total pore volume (V<sub>tot</sub>) increased by 2.5-fold from 450 to 1000 °C. At higher

carbonization temperatures, we attribute increased surface area and pore volume to increased PTA decomposition and volatilization. As PTA (a porogen) volatilizes, we expect a greater number of pores and larger pore radii (more surface area). Further, the V-t method demonstrated that micropores are less dominant when carbonized at 1000 °C. Better agreement between  $S_{\text{BET}}$  and  $S_{\text{ext}}$  for 1000 °C composites indicates less microporosity than for 450 °C composites, where the t-plot method defines  $S_{\text{micro}} = S_{\text{BET}} - S_{\text{ext}}$ . While the V-t and BJH methods are less complex than statistic-based density functional theory (DFT),<sup>7, 11-13</sup> the two widely applied methods provide micropore and mesopore characterization for the CNF/TiO<sub>2</sub> composites that agrees with the total surface area from the multi-point BET method.

*Electrochemical characterization. Diffusion coefficient (D).* Diffusive processes may govern the limiting current and kinetics in an electrochemical system by restricting ion transport to and from electrode surface. To quantify mass transfer effects with the CNF/TiO<sub>2</sub> composites, the diffusion coefficient (D) was determined by the data-based method provided by Nguyen and Breitung.<sup>14</sup> The method was developed to determine diffusion parameters for adsorbed gases on porous solids with PEIS data resembling the Randles circuit model with a finite-length Warburg element. Diffusive processes become relevant in the low frequency range (< 10 Hz), the linear transition region where real and imaginary impedance values are equal in magnitude. This is also the region where the Warburg impedance, a function of the square root of angular frequency ( $\omega$ ), is represented. The limiting diffusion resistance ( $R_w$ ), or the Warburg coefficient ( $\sigma_w$ ), can be calculated using the impedance data in the transition region when a finite

diffusion layer thickness is assumed. Therefore, real impedance ( $Z'$ ) values from the data in the low frequency range were used to determine  $\sigma_w$ . The equation of the finite-length Warburg impedance ( $Z_{w-o}$ ) allows us to obtain  $\sigma_w$  from our PEIS data, which resembled the Randles circuit.<sup>14</sup>

$$Z_{w-o} = \frac{\sigma_w}{\sqrt{j\omega\tau_D}} \tanh(\sqrt{j\omega\tau_D}) \quad (3)$$

where  $\sigma_w$  is the Warburg coefficient,  $j = \sqrt{-1}$ ,  $\omega$  is the radial frequency (rad), and  $\tau_D$  is the diffusion time constant (s). Alternatively, equation 3 can be expressed as

$$Z''_{w-o} = -\frac{\sigma_w[\sinh(\sqrt{2\omega\tau_D}) - \sin(\sqrt{2\omega\tau_D})]}{\sqrt{2\omega\tau_D}[\cosh(\sqrt{2\omega\tau_D}) + \cos(\sqrt{2\omega\tau_D})]} \quad (4)$$

which can be simplified to

$$Z''_w(\omega) = -\sigma_w \cdot f \left( \frac{1}{\sqrt{\omega}} \right) \quad (5)$$

where the slope,  $\sigma_w$ , is obtained from the imaginary Warburg impedance ( $Z''_w$ ) versus  $\omega^{0.5}$  plot. For  $\sigma_w$  in the low frequency transition range,  $Z'$  was substituted for  $Z''_w$ . Values for  $\sigma_w$  are only reported if the linear fit provides  $R^2 \geq 0.95$ . This  $R^2$  value is appropriate due to the sensitivity of PEIS measurements at low frequencies.

After  $\sigma_w$  was obtained, Equation 6 was used to calculate  $D$ ,

$$D = \frac{R^2 T^2}{2A^2 F^4 C^2 \sigma_w^2} \quad (6)$$

where  $R$  is the universal gas constant ( $8.314 \text{ J mol}^{-1}\text{K}^{-1}$ ),  $T$  is absolute temperature (K),  $F$  is the Faraday constant ( $\text{C mol}^{-1}$ ),  $C$  is the ion concentration ( $\text{mol L}^{-1}$ ), and  $\sigma_w$  is the Warburg coefficient ( $\Omega \text{ s}^{-0.5}$ ).<sup>15-17</sup> Equation 6 is traditionally used to determine coefficients for the lithium ion ( $\text{Li}^+$ ) in electrodes; however, it is assumed this equation holds for the potassium ion ( $\text{K}^+$ ) because both  $\text{Li}^+$  and  $\text{K}^+$  are expected to behave similarly as alkali metal ions. Similarly, this equation was applied to determine the

diffusion coefficient of chloride in concrete.<sup>18</sup> D values for the CNF/TiO<sub>2</sub> composite electrodes (**Table S5**) are equivalent to those reported by Lin and colleagues for composite lithium electrodes ( $10^{-14} \leq D \leq 10^{-16}$ ).<sup>19</sup>

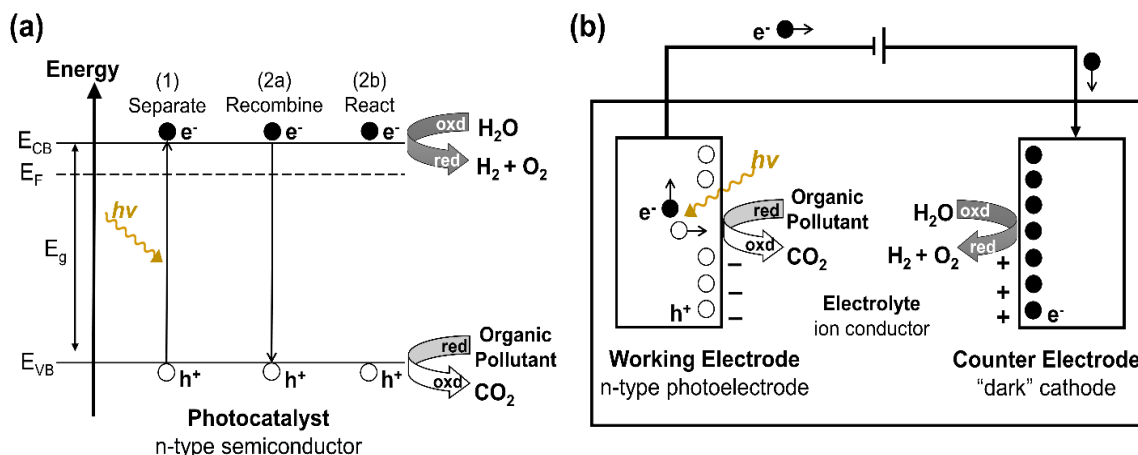


**Figure S1.** Schematic diagrams illustrating pollutant transformation via (a) photocatalytic (PC) and (b) photoelectrochemical (PEC) processes involving a n-type semiconductor. In contrast to PC processes, which suspend the semiconductor in solution, the semiconductor is fixed on a substrate in PEC processes. Conduction band ( $E_{CB}$ ), Fermi level ( $E_F$ ), Energy band gap ( $E_g$ ), and Valence band ( $E_{VB}$ ), hole ( $h^+$ ), electron ( $e^-$ ).

Increasing thickness  
→

Increasing wt% P25  
↓

0 wt% P25 / 0.15 g PAN	0 wt% P25 / 0.30 g PAN	0 wt% P25 / 0.45 g PAN
30 wt% P25 / 0.15 g PAN	30 wt% P25 / 0.30 g PAN	30 wt% P25 / 0.45 g PAN
50 wt% P25 / 0.15 g PAN	50 wt% P25 / 0.30 g PAN	50 wt% P25 / 0.45 g PAN
70 wt% P25 / 0.15 g PAN	70 wt% P25 / 0.30 g PAN	70 wt% P25 / 0.45 g PAN

**Figure S2.** Matrix of electrospinning precursor solution compositions illustrating the 12 different formulations fabricated and characterized herein. Each cell represents a single formulation (e.g., 0 wt%  $TiO_2$  / 0.15 g PAN, 0 wt%  $TiO_2$  / 0.30 g PAN).



**Figure S3.** Photograph of the lab-scale, custom-built electrospinning enclosure used for nanofiber fabrication, with key components labeled.

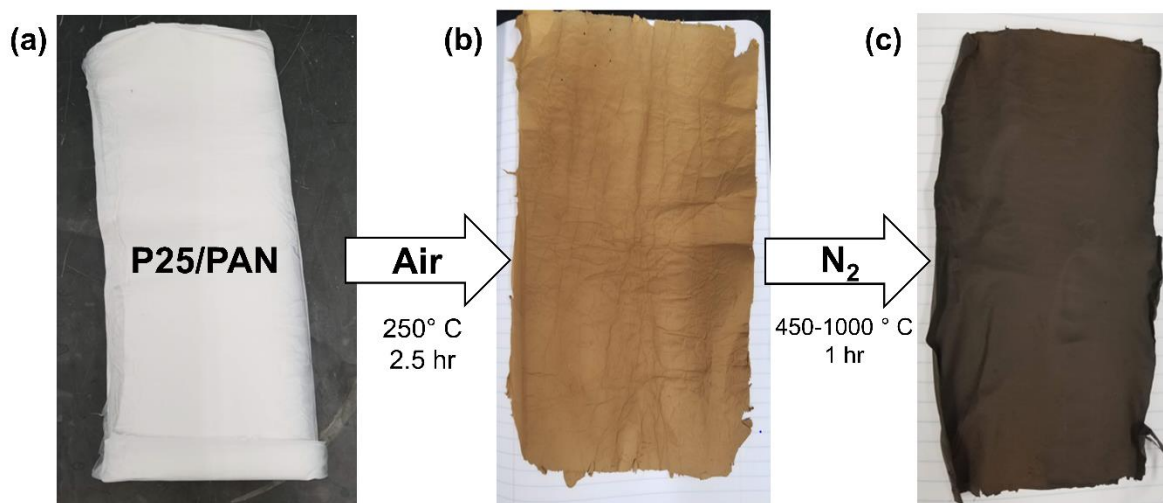


**Figure S4.** Changes in material character and appearance resulting from steps in the fabrication process, where the CNF material is shown after: (a) electrospinning, (b) oxidative stabilization under air, and (c) carbonization under  $N_2$ . Electrode fabrication is complete when carbonized. Total mass decreased with each successive synthesis step (electrospinning, stabilization, carbonization) as follows: total mass as deposited from electrospinning decreased by  $16 (\pm 2)\%$  after stabilization, whereas (with respect to stabilization) total mass further decreased by  $34 (\pm 5)\%$  when carbonized at the highest temperature ( $1000\text{ }^\circ\text{C}$ ).

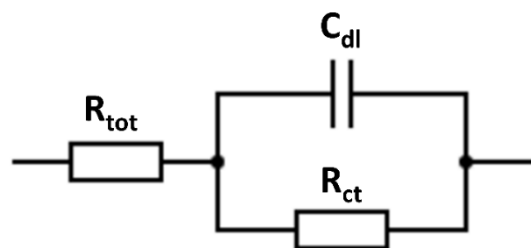


**Figure S5.** Representation of the Simple Randles model circuit, where  $R_{tot}$  is the total resistance,  $R_{ct}$  is the charge transfer resistance, and  $C_{dl}$  is the double-layer capacitance.

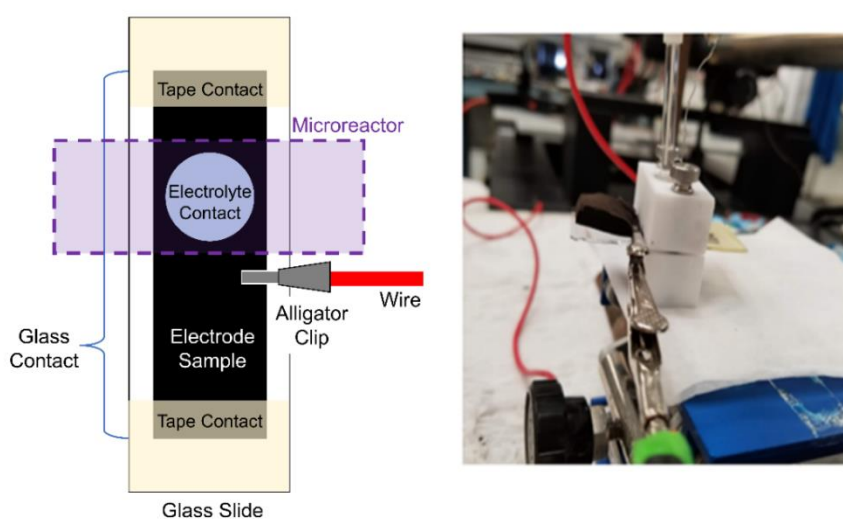


**Figure S6.** PEIS sample preparation top view (left) and side view (right) with key components labeled in the schematic on the left .

**Table S1.** Experimental parameters for all PEIS experiments.

Parameter	Specification
Initial frequency, $f_i$	7 MHz
Final frequency, $f_f$	1 Hz
Sampling frequency, $N_d$	15 pts per decade
Sinus amplitude, $V_a$	25 mV
Counter electrode, CE	Platinum wire
Reference electrode, RE	Ag/Ag-Cl
Working electrode, WE	CNF electrode
Electrolyte	0.5 M phosphate buffer, pH 7.4

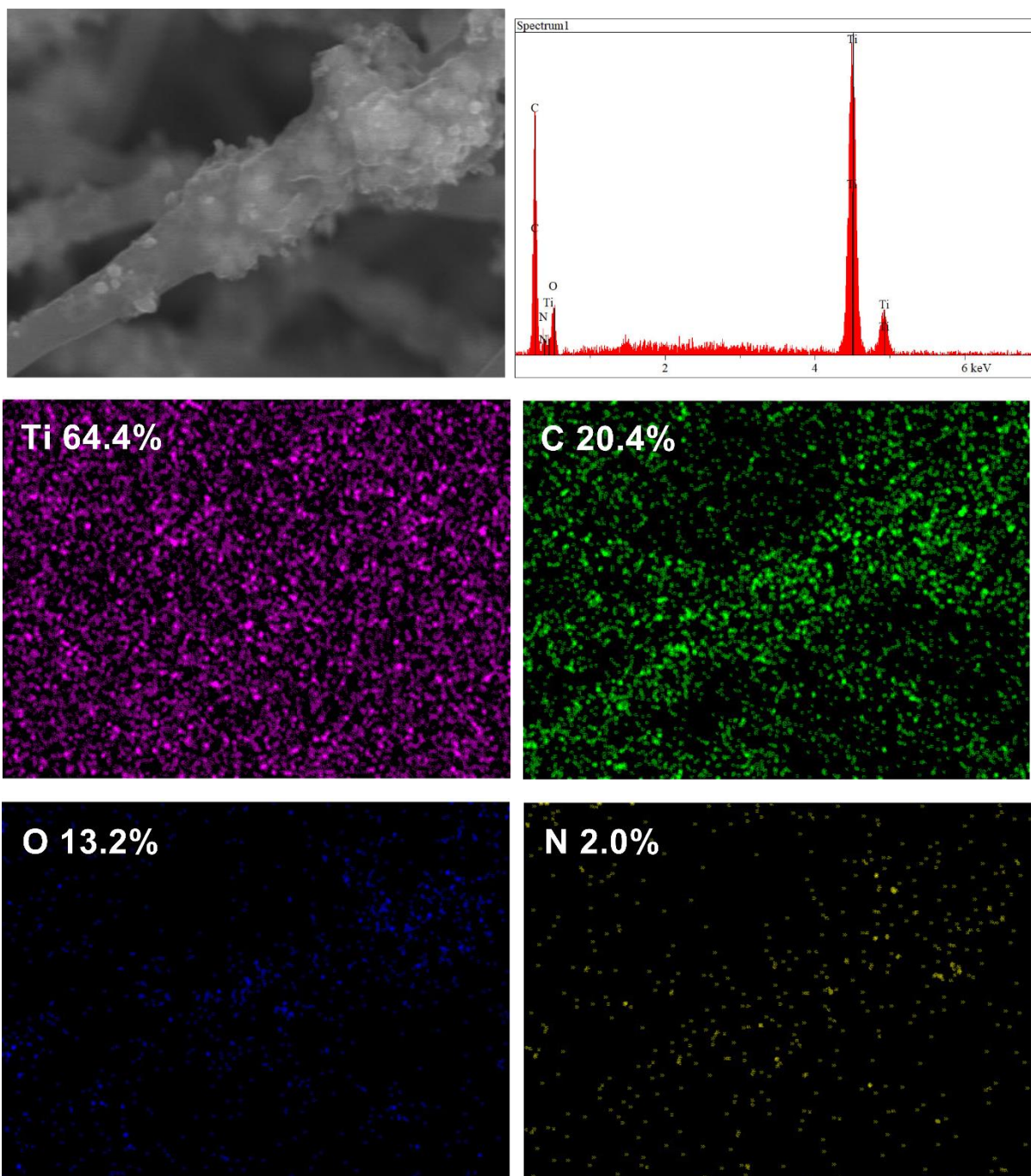
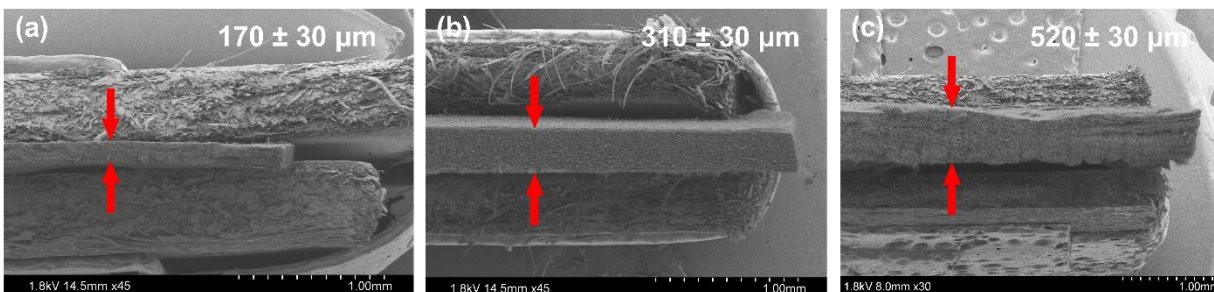


**Figure S7.** SEM image (50 $\times$ , 15 kV) and corresponding EDS elemental maps of the optimal CNF/TiO<sub>2</sub> composite (0.45 g PAN / 50 wt% TiO<sub>2</sub> / 1000  $^{\circ}$ C).



**Figures S8.** Cross-sectional SEM images of the 50 wt% TiO<sub>2</sub> composite (carbonized at 450 °C) as a function of deposited PAN mass. Images are shown for composites fabricated using (a) 0.15, (b) 0.30, (c) 0.45 g PAN. The distance between arrows identifies the electrode thickness as measured. Values shown are mean and standard deviations of n = 22 measurements.

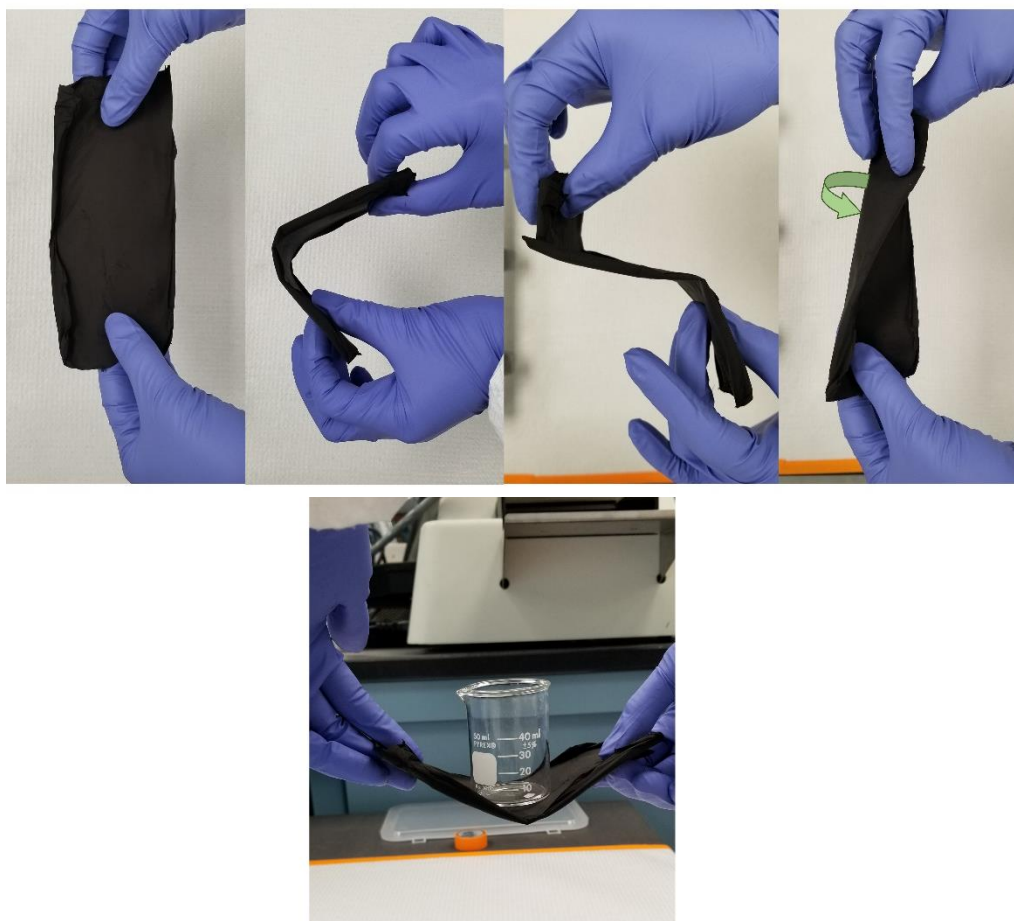


**Figure S9.** Examples of material handling (simple bending and rotational tests) to demonstrate bulk mechanical durability and strength for 0.45 g PAN / 50 wt% TiO<sub>2</sub> composites carbonized at 1000 °C.

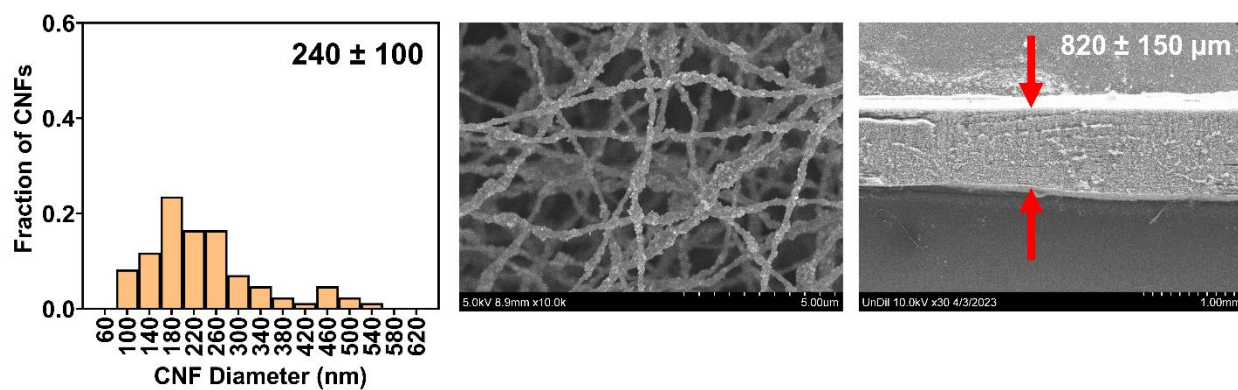


**Figure S10.** SEM images of 50 wt% TiO<sub>2</sub> composites fabricated with 0.45 g PAN and carbonized at 1000 °C. Value in histogram represents mean fiber diameter and standard deviation ( $n = 85$ ). Value in cross-sectional image represents mean thickness and standard deviation ( $n = 22$ ). Distance between arrows identifies the electrode thickness as measured.

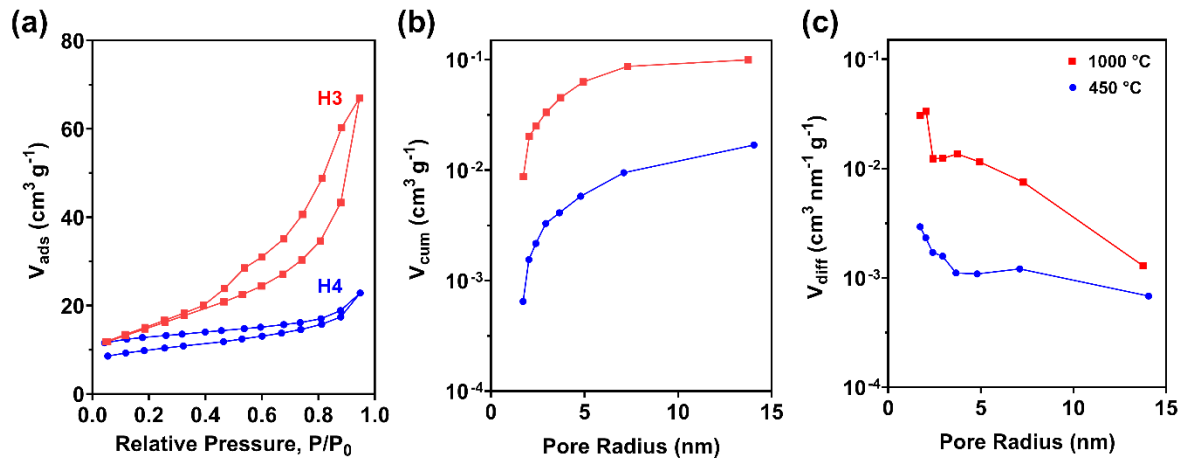


**Figure S11.** (a)  $\text{N}_2$  adsorption-desorption isotherms for 0.45 g PAN / 50 wt%  $\text{TiO}_2$  composites carbonized at 1000 °C (red) and 450 °C (blue), which are consistent with the hysteresis modes (e.g., H3 or H4) as indicated. (b, c) Resulting pore distribution derived via BJH method from the corresponding desorption isotherms with respect to cumulative volume ( $V_{cum}$ ) and differential volume ( $V_{diff}$ )

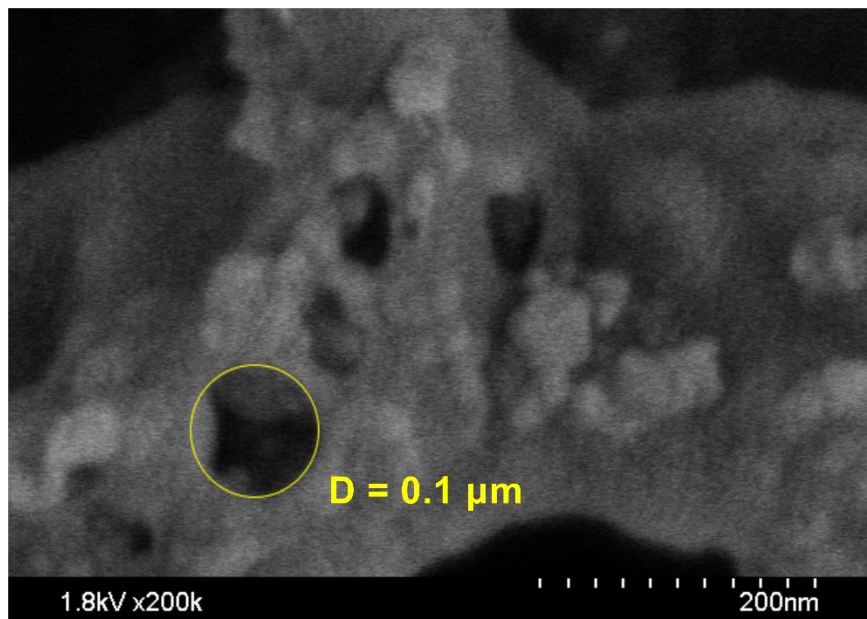


**Figure S12.** Large mesopore on 0.45 g PAN / 50 wt%  $\text{TiO}_2$  / 1000 °C fiber surface as observed from SEM imaging.

**Table S2.** Specific surface area and total pore volume for 0.45 g PAN / 50 wt% TiO<sub>2</sub> composites carbonized at 450 and 1000 °C as obtained from N<sub>2</sub> adsorption-desorption isotherm analysis.

Carbonization Temp (°C)	S <sub>BET</sub> (m <sup>2</sup> g <sup>-1</sup> )	S <sub>EXT</sub> (m <sup>2</sup> g <sup>-1</sup> )	S <sub>micro</sub> (m <sup>2</sup> g <sup>-1</sup> )	S <sub>meso</sub> (m <sup>2</sup> g <sup>-1</sup> )	V <sub>tot</sub> (cm <sup>3</sup> g <sup>-1</sup> )
450	31 ± 2	21 ± 2	11 ± 5	8 ± 3	0.04 ± 0.007
1000	54 ± 1	47 ± 2	7 ± 3	50 ± 4	0.10 ± 0.001

S<sub>BET</sub>, Multi-point BET

S<sub>EXT</sub>, External surface area (t-area) via the V-t method

S<sub>micro</sub>, Microporous surface area where S<sub>micro</sub> = S<sub>BET</sub> - S<sub>EXT</sub>

S<sub>meso</sub>, Mesoporous surface area via the BJH method

V<sub>tot</sub>, Total pore volume estimated at P/P<sub>0</sub> ≈ 0.95

**Table S3.** Graphitic character (R-value) and in-plane crystalline size (L<sub>a</sub>) from Raman spectroscopy for 0.45 g PAN / 50 wt% TiO<sub>2</sub> composites with carbonization temperature.

Carbonization Temp (°C)	D-band Intensity (1355 cm <sup>-1</sup> )	G-band Intensity (1575 cm <sup>-1</sup> )	R-value	L <sub>a</sub> (nm)
450	9.32E+04	7.06E+04	1.32	3.3
575	4.47E+04	3.32E+04	1.35	3.3
750	2.03E+04	2.05E+04	0.99	4.3
1000	1.34E+04	1.66E+04	0.81	5.4

**Table S4.** Average charge transfer (R<sub>ct</sub>) and total (R<sub>tot</sub>) resistance (with standard deviations) from five replicates per sample with 0.45 g PAN composites (carbonized at 450 °C) fabricated over a six-month period. The number of samples (n) is provided.

Wt% P25	R <sub>ct</sub> (Ω cm <sup>2</sup> )	R <sub>tot</sub> (Ω cm <sup>2</sup> )	n
0	680 ± 240	850 ± 240	2
30	330 ± 80	420 ± 110	3
50	300 ± 50	390 ± 70	4
70	460 ± 10	580 ± 10	2

**Table S5.** Diffusion coefficients ( $D$ ) for CNF/TiO<sub>2</sub> electrodes as determined by PEIS data. The coefficient for Kynol Activated Carbon Cloth 5092-10 was also determined using our PEIS set-up. Electrolyte: 0.5 M phosphate buffer, pH 7.4.

TiO <sub>2</sub> Content (wt. %)	Carbonization Temp (°C)	Diffusion Coefficient (cm <sup>2</sup> s <sup>-1</sup> )
0	450	$8.9 \times 10^{-16} \pm 1.8 \times 10^{-16}$
30	450	$1.2 \times 10^{-15} \pm 4.0 \times 10^{-16}$
50	450	$4.6 \times 10^{-14} \pm 4.2 \times 10^{-14}$
50	1000	$2.7 \times 10^{-08} \pm 1.4 \times 10^{-08}$
70	450	$1.1 \times 10^{-15} \pm 3.7 \times 10^{-16}$
Kynol 5092-10	--	$9.4 \times 10^{-10} \pm 8.4 \times 10^{-10}$

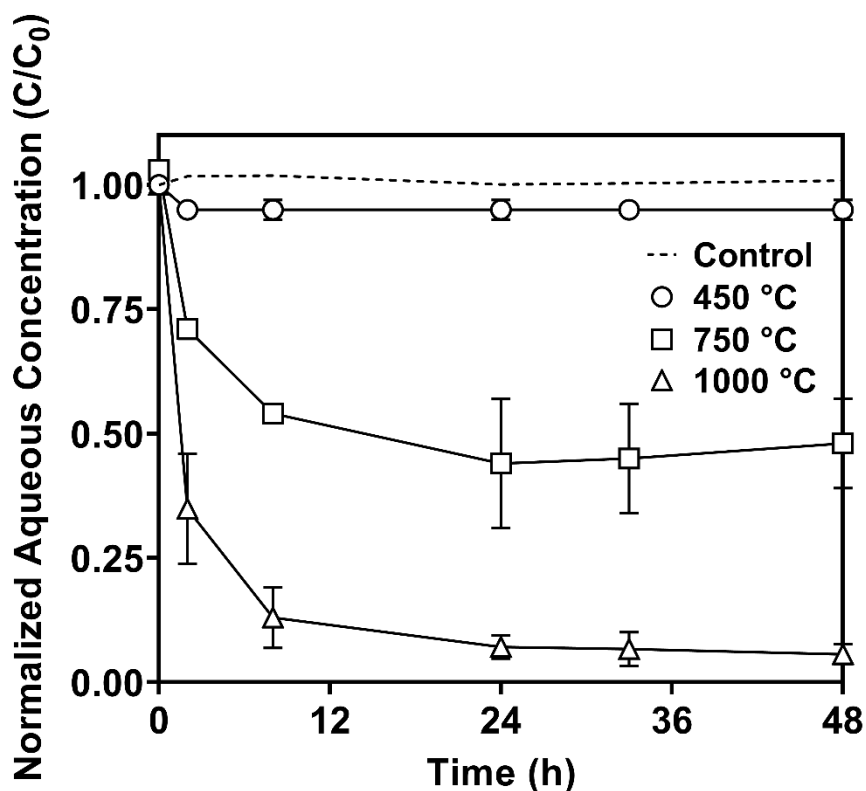


**Figure S13.** Sorption of CBZ on CNF/TiO<sub>2</sub> (50 wt%) composites carbonized at 450, 750, and 1000 °C over 48 h. Composite and solution ( $C_0 = 10 \mu\text{M}$  CBZ) were contained in a 40 mL amber glass vial that was sealed with a Teflon-lined screw cap and tumbled slowly end-over-end for the entire sampling period.

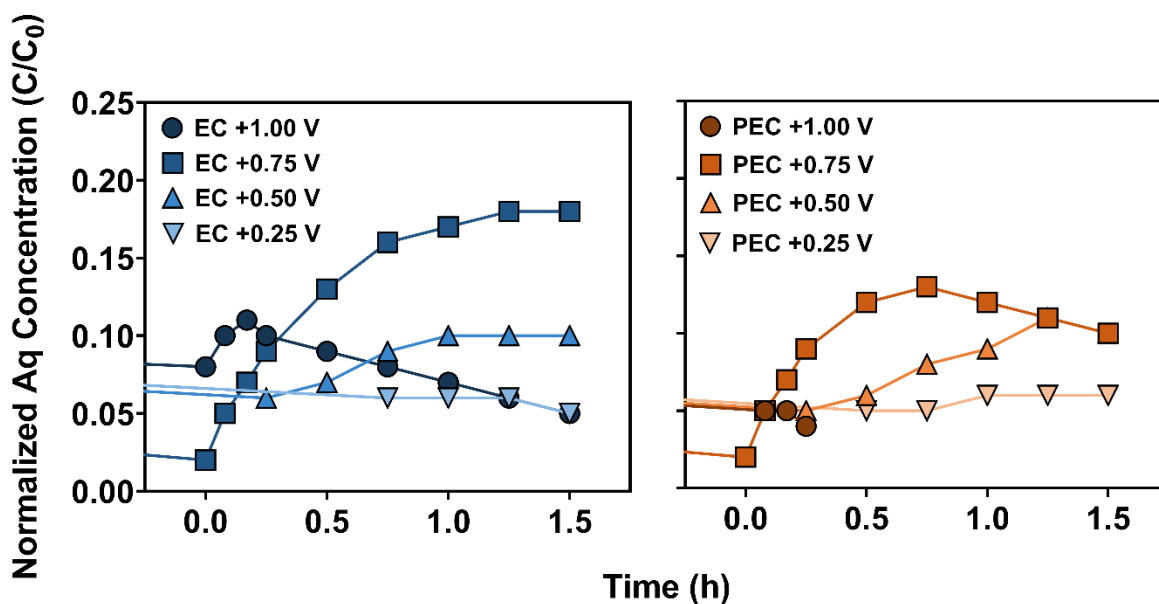


**Figure S14.** Normalized ( $C/C_0$ ) aqueous (Aq) CBZ concentration ( $C_0 = 10 \mu\text{M}$  CBZ) observed during the transformation period for the optimal CNF/TiO<sub>2</sub> composite (0.45 g PAN / 50 wt% TiO<sub>2</sub> / 1000 °C) in electrochemical (EC; left) and photoelectrochemical (PEC; right) systems. Four different potentials (V vs Ag/AgCl) were selected to investigate CBZ transformation. For EC transformation (left) at low potential (+0.25 V), aqueous CBZ was not detected until 45 minutes after transformation start, and its concentration remained near constant for the remainder of the transformation experiment ( $C/C_0 \approx 0.05$ ). For EC transformation at midscale potentials (+0.50, 0.75 V), aqueous CBZ concentration actually increased over time during the transformation period, which we attribute to the charging on the electrode surface in response to the applied potential that promoted release of the previously bound CBZ. At the highest potential (+1.00 V) explored in EC experiments, an initial period of CBZ release (~10 minutes) was followed by a steady decrease in aqueous CBZ concentration over the remaining time. Similar potential dependent trends in aqueous CBZ concentration were also observed during the PEC transformation period (right). At +0.25 and 0.50 V, aqueous concentrations of CBZ followed the same behavior observed in EC systems, with nearly constant concentration (at  $C/C_0 \sim 0.05$ ) in +0.25V and steadily increasing concentration at +0.50V. For PEC at +0.75 V, dissolved CBZ concentration initially increased (reaching a maximum after 30 minutes) before decreasing over the remainder of the 60 minutes transformation period, behavior that is distinct from that observed in the analogous EC system. Finally, for PEC systems at +1.00 V, aqueous CBZ remained small ( $C/C_0 < 0.05$ ) and was not detected after the first 15 minutes of the transformation period; notably, aqueous CBZ was detectable over the entire transformation period in the EC system at +1.00 V.

**Table S6.** Rate constants and corresponding half-life ( $t_{1/2}$ ) from previously published literature for carbamazepine (CBZ) degradation via various advanced treatment systems. Reference number corresponds to that provided in the manuscript. Results are shown for advanced oxidation processes (AOPs), photocatalytic treatment systems (PC), and electrochemical treatment systems (EC). Experimental conditions corresponding to each rate constant are provided.

System Type	Oxidation Catalyst / Material	Rate Constant ( $\text{min}^{-1}$ )	$t_{1/2}$ (min)	Experimental Conditions	Ref
AOP	UV/H <sub>2</sub> O <sub>2</sub>	0.04	17.6	[CBZ] = 4.2 $\mu\text{M}$ ; Catalyst dose = 10 mM H <sub>2</sub> O <sub>2</sub> ; Light = 30 W Hg lamp	76
AOP	UV/TiO <sub>2</sub>	0.13	5.2	[CBZ] = 4.2 $\mu\text{M}$ ; Catalyst dose = 2.0 g/L TiO <sub>2</sub> ; Light = 30 W Hg lamp	76
AOP	UV/Fenton	0.25	2.7	[CBZ] = 4.2 $\mu\text{M}$ ; Catalyst dose = 2.0 mM Fe <sup>2+</sup> ; Light = 30 W Hg lamp	76
PC	UV only	0.01	84.9	[CBZ] = 4.2 $\mu\text{M}$ ; Light = 30 W Hg lamp	76
PC	Ag <sub>3</sub> PO <sub>4</sub> /GO	0.12	5.8	[CBZ] = 21.2 $\mu\text{M}$ ; Catalyst dose = 0.5 g/L; Light intensity = 5.86 mW cm <sup>-2</sup>	44
PC	TiO <sub>2</sub> NFs	0.012	55.9	[CBZ] = 10 $\mu\text{M}$ ; Light intensity = 3.33E-4 E min <sup>-1</sup> L <sup>-1</sup>	45
EC	Nb/BDD	0.19	3.7	[CBZ] = 10 $\mu\text{M}$ ; Supporting electrolyte = 14 mM NaCl; Current = 1.0 A	77
EC	Ti/PbO <sub>2</sub>	0.021	33.0	[CBZ] = 42 $\mu\text{M}$ ; Supporting electrolyte = 400 mg/L Na <sub>2</sub> SO <sub>4</sub> ; Current = 2.0 A	78

## REFERENCES

1. AEROXIDE®, AERODISP®, and AEROPERL® Titanium Dioxide as Photocatalyst: Technical Information 1243
2. K. T. Peter, J. D. Vargo, T. P. Rupasinghe, A. De Jesus, A. V. Tivanski, E. A. Sander, N. V. Myung and D. M. Cwiertny, Synthesis, Optimization, and Performance Demonstration of Electrospun Carbon Nanofiber-Carbon Nanotube Composite Sorbents for Point-of-Use Water Treatment, *ACS Appl Mater Interfaces*, 2016, **8**, 11431-11440.
3. M. Kruk, M. Jaroniec and Y. Berezniński, Adsorption Study of Porous Structure Development in Carbon Blacks, *Journal of Colloid and Interface Science*, 1996, **182**, 282-288.
4. A. Galarneau, F. Villemot, J. Rodriguez, F. Fajula and B. Coasne, Validity of the t-plot Method to Assess Microporosity in Hierarchical Micro/Mesoporous Materials, *Langmuir*, 2014, **30**, 13266-13274.
5. A. Daraghmeh, S. Hussain, I. Saadeddin, L. Servera, E. Xuriguera, A. Cornet and A. Cirera, A Study of Carbon Nanofibers and Active Carbon as Symmetric Supercapacitor in Aqueous Electrolyte: A Comparative Study, *Nanoscale Research Letters*, 2017, **12**, 639.
6. E. P. Barrett, L. G. Joyner and P. P. Halenda, The Determination of Pore Volume and Area Distributions in Porous Substances. I. Computations from Nitrogen Isotherms, *Journal of the American Chemical Society*, 1951, **73**, 373-380.
7. R. Bardestani, G. S. Patience and S. Kaliaguine, Experimental methods in chemical engineering: specific surface area and pore size distribution measurements—BET, BJH, and DFT, *The Canadian Journal of Chemical Engineering*, 2019, **97**, 2781-2791.
8. H. Hatta, T. Aoi, I. Kawahara and Y. Kogo, Tensile Strength of Carbon–Carbon Composites: II – Effect of Heat Treatment Temperature, *Journal of Composite Materials*, 2004, **38**, 1685-1699.
9. M. Borisover, M. Sela and B. Chefetz, Enhancement effect of water associated with natural organic matter (NOM) on organic compound-NOM interactions: A case study with carbamazepine, *Chemosphere*, 2011, **82**, 7.
10. K. S. W. Sing, Reporting physisorption data for gas/solid systems with special reference to the determination of surface area and porosity (Recommendations 1984), *Pure and Applied Chemistry*, 1985, **57**, 603-619.
11. O. Šolcová, L. Matějová and P. Schneider, Pore-size distributions from nitrogen adsorption revisited: Models comparison with controlled-pore glasses, *Applied Catalysis A: General*, 2006, **313**, 167-176.
12. J. Landers, G. Y. Gor and A. V. Neimark, Density functional theory methods for characterization of porous materials, *Colloids and Surfaces A: Physicochemical and Engineering Aspects*, 2013, **437**, 3-32.
13. K. Sing, The use of nitrogen adsorption for the characterisation of porous materials, *Colloids and Surfaces A: Physicochemical and Engineering Aspects*, 2001, **187-188**, 3-9.
14. T. Q. Nguyen and C. Breitkopf, Determination of Diffusion Coefficients Using Impedance Spectroscopy Data, *Journal of The Electrochemical Society*, 2018, **165**, E826-E831.

15. C. Chang, J. Dong, L. Guan and D. Zhang, Enhanced Electrochemical Performance of  $\text{Li}_{1.27}\text{Cr}_{0.2}\text{Mn}_{0.53}\text{O}_2$  Layered Cathode Materials via a Nanomilling-Assisted Solid-state Process, *Materials (Basel)*, 2019, **12**.
16. D. Luo, S. Fang, L. Yang and S.-i. Hirano, Improving the electrochemical performance of layered Li-rich transition-metal oxides by alleviating the blockade effect of surface lithium, *Journal of Materials Chemistry A*, 2016, **4**, 5184-5190.
17. Q. Cao, H. P. Zhang, G. J. Wang, Q. Xia, Y. P. Wu and H. Q. Wu, A novel carbon-coated  $\text{LiCoO}_2$  as cathode material for lithium ion battery, *Electrochemistry Communications*, 2007, **9**, 1228-1232.
18. R. Vedalakshmi, V. Saraswathy, H.-W. Song and N. Palaniswamy, Determination of diffusion coefficient of chloride in concrete using Warburg diffusion coefficient, *Corrosion Science*, 2009, **51**, 1299-1307.
19. C. Lin, X. Fan, Y. Xin, F. Cheng, M. O. Lai, H. Zhou and L. Lu,  $\text{Li}_4\text{Ti}_5\text{O}_{12}$ -based anode materials with low working potentials, high rate capabilities and high cyclability for high-power lithium-ion batteries: a synergistic effect of doping, incorporating a conductive phase and reducing the particle size, *J. Mater. Chem. A*, 2014, **2**, 9982-9993.